Shortwave aerosol radiative forcing over cloud-free oceans from Terra: 2. Seasonal and global distributions

Jianglong Zhang,[1,2] and Sundar A. Christopher
Department of Atmospheric Sciences, University of Alabama, Huntsville, Alabama, USA

Lorraine A. Remer and Yoram J. Kaufman
NASA Goddard Space Flight Center Data Center, Greenbelt, Maryland, USA

Received 12 May 2004; revised 18 August 2004; accepted 1 December 2004; published 9 March 2005.

[1] Using 10 months of collocated Clouds and the Earth's Radiant Energy System (CERES) scanner and Moderate Resolution Imaging Spectroradiometer (MODIS) aerosol and cloud data from Terra, we provide estimates of the shortwave aerosol direct radiative forcing (SWARF) and its uncertainties over the cloud-free global oceans. Newly developed aerosol angular distribution models (ADMs) (Zhang et al., 2005), specifically for different sea surface conditions and aerosol types, are used for inverting the CERES observed radiances to shortwave fluxes while accounting for the effect of aerosol optical properties on the anisotropy of the top of atmosphere (TOA) shortwave radiation fields. The spatial and seasonal distributions of SWARF are presented, and the MODIS retrieved aerosol optical depth ($\tau_{0.55}$) and the independently derived SWARF show a high degree of correlation and can be estimated using the equation SWARF = 0.05 − 74.6 $\tau_{0.55}$ + 18.2 $\tau_{0.55}^2$ W m^{-2} ($\tau_{0.55} < 0.8$). The instantaneous TOA SWARF from Terra overpass time is −6.4 ± 2.6 W m^{-2} for cloud-free oceans. Accounting for sample biases and diurnal averaging, we estimate the SWARF over cloud-free oceans to be −5.3 ± 1.7 W m^{-2}, consistent with previous studies. Our study is an independent measurement-based assessment of cloud-free aerosol radiative forcing that could be used as a validation tool for numerical modeling studies.

Citation: Zhang, J., S. A. Christopher, L. A. Remer, and Y. J. Kaufman (2005), Shortwave aerosol radiative forcing over cloud-free oceans from Terra: 2. Seasonal and global distributions, *J. Geophys. Res.*, *110*, D10S24, doi:10.1029/2004JD005009.

1. Introduction

[2] Owing to their significance in climate change studies [*Intergovernmental Panel on Climate Change* (*IPCC*), 2001], aerosols and their radiative effects have been studied through various methods [e.g., *Hansen et al.*, 1998; *Haywood et al.*, 1999]. Commonly used approaches to study the effect of aerosols on climate include either simple radiative transfer equations [e.g., *Penner et al.*, 1994] or complex general circulation models [*Hansen et al.*, 1998]. However, satellite observations have also been used to study the shortwave aerosol radiative forcing (SWARF) over cloud-free conditions [*Loeb and Kato*, 2002; *Christopher and Zhang*, 2002, 2004]. In these studies, satellite broadband observations from either the Earth Radiation Budget Experiment (ERBE) or Clouds and the Earth's Radiant Energy System (CERES) are classified into three groups of data including "clear," "cloud-free aerosol skies" and "cloudy skies" through the use of additional multispectral satellite observations. The SWARF over cloud-free skies is then derived by removing the clear sky component from the top of atmosphere (TOA) fluxes. Since the CERES has a large footprint on the order of 20 km at nadir on Terra, additional finer spatial resolution satellite observations are needed to obtain aerosol and cloud properties within the CERES footprint.

[3] Using a similar approach from the Visible Infrared Scanner (VIRS) and CERES data on board the Tropical Rainfall Measuring Mission (TRMM), *Christopher et al.* [2000] studied the SWARF over both land and ocean. *Loeb and Kato* [2002] extended this study using nine months of collocated VIRS and CERES data, and reported diurnally averaged SWARF of −4.6 W m^{-2} over the tropical oceans. However, the VIRS was not designed for aerosol studies and has several limitations including limited number of spectral channels, limited spatial coverage (only 37N−37S), and coarse spatial resolution of 2 km when compared with other current imagers such as Moderate Resolution Imaging Spectroradiometer (MODIS).

[4] The recently launched Terra and Aqua satellites provide an excellent opportunity for studying both aerosol and SWARF using space observations. Onboard these

[1] Now at Naval Research Laboratory, Monterey, California, USA.
[2] Visiting scientist from University Corporation for Atmospheric Research, Boulder, Colorado, USA.

0148-0227/05/2004JD005009

satellites, the Moderate Resolution Imaging Spectroradiometer (MODIS) has a total of 36 channels with improved spatial, spectral and radiometric resolutions when compared with previous imagers [*King et al.*, 1992]. A major goal of MODIS is to characterize the spatial distribution of aerosols and clouds and their optical properties. Over global oceans, the MODIS is used to retrieve aerosol optical depth and aerosol particle size information and have been intensively validated against ground and insitu measurements [e.g., *Remer et al.*, 2002]. Also on board Terra, the CERES, which is a broadband instrument, can be used to obtain TOA outgoing shortwave and longwave fluxes. The MODIS cloud and aerosol information and the CERES TOA fluxes have been merged together to form the CERES Single Scanner Footprint (SSF) data [*Loeb and Kato*, 2002], which can be used to examine the effect of aerosols on the Earth-atmosphere system. Since the CERES does not observe SW fluxes directly, Angular Dependence Models (ADMs) are used for inverting the observed radiance to TOA flux for a given scene [*Wielicki et al.*, 1996]. Using ten months of MODIS and CERES data from Terra, new aerosol ADMs have been developed specifically for satellite SWARF studies and is an improvement over the previous ERBE and TRMM ADMs [*Zhang et al.*, 2005].

[5] In this paper, we examine the SWARF over global cloud-free oceans and the seasonal and regional distributions of SWARF are also presented. Different from our previous efforts [*Christopher and Zhang*, 2002], the effects of solar zenith angle, clear-sky bias, diurnal averaging and the ratio of fine mode to total aerosol optical depth on the satellite-derived SWARF are investigated.

2. Data Sets

[6] The details of the CERES and MODIS data sets are discussed in detail in the work of *Zhang et al.* [2005] and only a brief summary is provided here. We used ten months (November 2000 to August 2001) of the CERES SSF product that contains the point spread function weighted aerosol and cloud properties [*Loeb et al.*, 2003] including the aerosol optical depth and the ratio (η) of fine aerosol to total aerosol optical depth at 0.47, 0.55 and 0.67 μm [*Kaufman et al.*, 2005; *Remer et al.*, 2002]. The MODIS retrieved aerosol optical properties at 0.55 μm ($\tau_{0.55}$) are used in this study and recent studies show that the MODIS retrieved aerosol optical depth values ($\tau_{0.55}$) are within the expected uncertainties of $\pm 0.03 \pm 0.05\ \tau_{0.55}$ over the global oceans [*Remer et al.*, 2002]. In this study, only CERES observations over cloud-free oceans are used and we require the CERES pixels to be at least 99.9% cloud-free as determined by MODIS data.

3. Methods and Results

[7] In a companion paper [*Zhang et al.*, 2005], we describe the angular models that were developed for converting the CERES measured radiances to TOA fluxes for cloud-free pixels. The new aerosol ADMs are built as functions of SSM/I wind speed, the ratio of fine mode AOT to total AOT (η), and the MODIS aerosol optical thickness. In previous studies [e.g., *Loeb and Kato*, 2002; *Christopher and Zhang*, 2002], over cloud-free oceans, there was only one set of ADMs available and aerosol darkening effect over glint regions and aerosol brightening effect over nonglint regions are not considered and therefore, the derived SWARF could be overestimated [*Zhang et al.*, 2005]. For the TRMM ADMs, only one aerosol model (maritime tropical aerosol model) for correcting the effects of aerosols on the angular distribution pattern of TOA SW radiation fields is assumed, and therefore the SWARF could be underestimated. In this study, we compare the SWARF using ERBE, TRMM, and Terra ADMS over cloud-free oceans and examine the seasonal and spatial distribution of SWARF from the newly constructed ADMs.

[8] The SWARF is defined as the difference in the SW flux observed without (F_{clr}) and with (F_{aero}) the presence of aerosols [e.g., *Ackerman and Chung*, 1992; *Christopher and Zhang*, 2002] where F_{clr} is "clear-sky" flux that represents TOA CERES fluxes in cloud and aerosol-free conditions and F_{aero} is the observed cloud-free CERES TOA SW flux in the presence of aerosols. Both F_{clr} and F_{aero} are computed for every 2×2 degree latitude, longitude bins and due to the significant increase in pixel size as a function of scan angle, only the CERES pixels that have viewing zenith angle less than 60° and solar zenith angle less than 60° are used. The SWARF is derived by subtracting the F_{clr} of a 2×2 degree bin from the bin averaged cloud-free CERES flux.

[9] To obtain SWARF, the TOA SW fluxes in aerosol and cloud-free conditions are needed where F_{clr} is defined as the SW flux when MODIS $\tau_{0.55} = 0$. However, it is not possible to have observed scenes that have zero aerosol loading. Therefore, in this study, the F_{clr} is computed using the two steps. First, the seasonal mean F_{clr} values are constructed as functions of solar zenith angle (θ_o) and near surface wind speed. Owing to uncertainties in MODIS aerosol retrievals at very low optical depths [e.g., *Remer et al.*, 2002], it is difficult to isolate CERES pixels with zero $\tau_{0.55}$. Therefore we assume that for observations with $\tau_{0.55} < 0.2$, CERES fluxes and MODIS $\tau_{0.55}$ have a linear relationship [*Christopher and Zhang*, 2002] and for each θ_o and wind speed bin (ten θ_o and four wind speed bins), the linear regression relation (equation (1)) is computed using all cloud-free CERES pixels that have $\tau_{0.55} < 0.2$.

$$\text{SW flux} = F_{clr} + \text{slope}^* \tau_{0.55} \tag{1}$$

[10] The F_{clr} is obtained by extrapolating the regression relation back to zero $\tau_{0.55}$. Using this approach, lookup tables of F_{clr} and the slope of SW flux versus $\tau_{0.55}$ are established as functions of wind speed and θ_o. Therefore, for a given CERES observation, the F_{clr} can be obtained using the predetermined LUTs.

[11] Averaging over all solar zenith angle bins and all wind speed bins, the F_{clr} values are 70.4, 72.0 and 74.6 W m^{-2} for the Northern Hemisphere summer (June–July–August), spring (March–April–May), and winter (November–December–January–February) seasons, respectively. Owing to variations in oceanic and atmospheric conditions such as water vapor, F_{clr} also shows local variations. To account for these local variations, a correction factor is computed locally. For each bin, the mean SW flux, $\tau_{0.55}$, θ_o and wind speed for CERES pixels that have $\tau_{0.55} < 0.2$ are computed for each season. The mean θ_o and wind speed are used as indices to

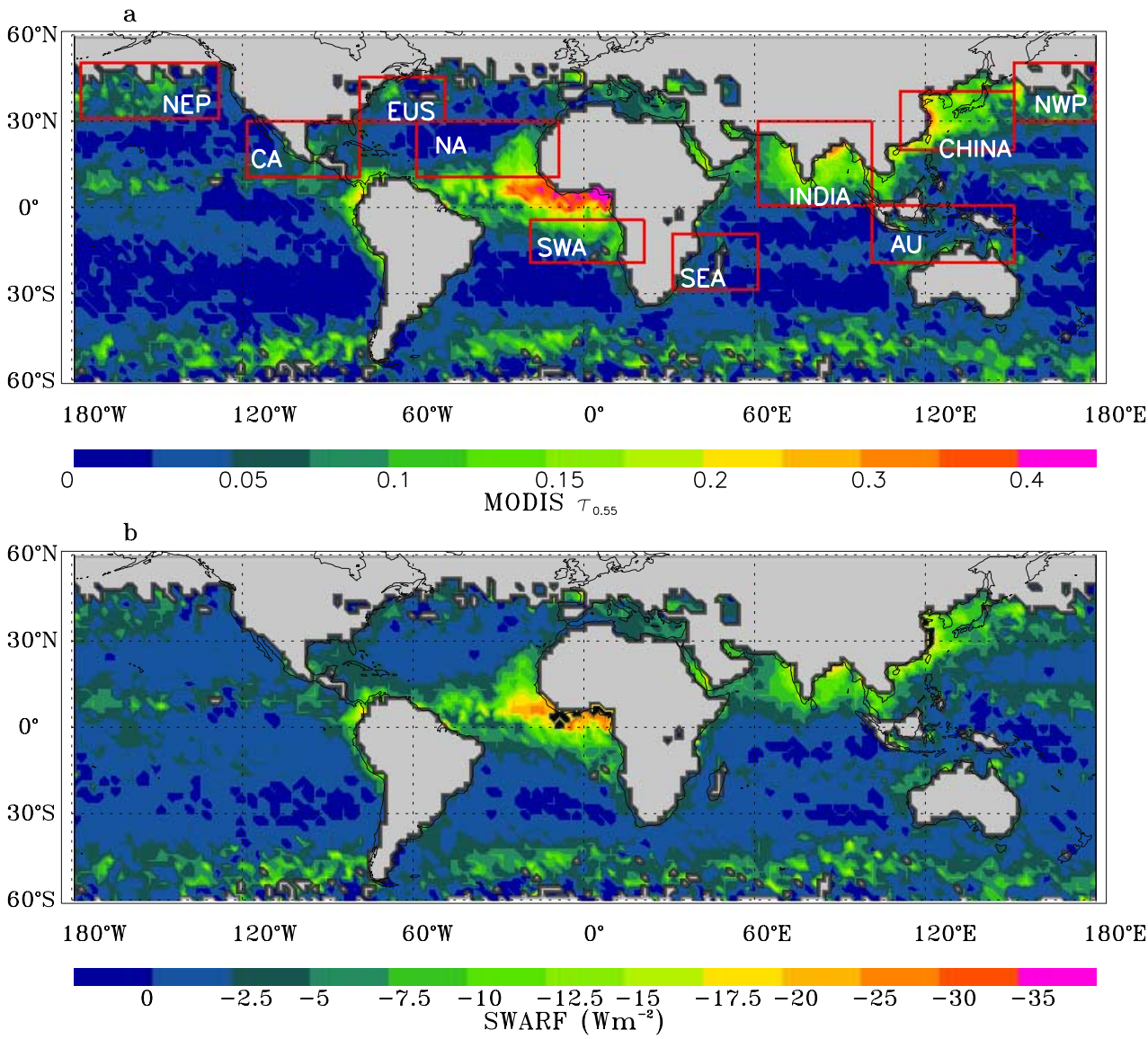

Figure 1. Spatial distribution of MODIS $\tau_{0.55}$ over CERES cloud-free oceans and the CERES derived SWARF for the three Northern Hemisphere seasons: (a and b) winter (November and December 2000 and January and February 2001), (c and d) spring (March, April, and May 2001), and (e and f) summer (June, July, and August 2001).

retrieve both F_{clr} and the slope of the regression relation from the predetermined LUTs. Using the retrieved regression relation, a new flux value is derived by inputting the averaged $\tau_{0.55}$ value. The difference between the averaged and derived fluxes (ΔF) is assumed to be from local variations and F_{clr} is therefore adjusted by adding the correction term ΔF that are the order of 1.71, 1.34 and 1.67 W m^{-2} for the winter, spring, and summer seasons, respectively.

[12] Figures 1a–1f show the global distribution of MODIS $\tau_{0.55}$ and CERES-derived SWARF over cloud-free oceans for winter, spring, and summer seasons. These values are called instantaneous because they are derived from the time of the satellite overpass. The geographical distribution of $\tau_{0.55}$ and CERES-derived SWARF are consistent, and regions with high $\tau_{0.55}$ are associated with regions of high SWARF. For example, in winter, both high aerosol loading and high SWARF are observed over the west coast of Africa, the Indian Ocean and the east coast of Asia. Figure 2 shows the scatterplot of $\tau_{0.55}$ versus SWARF for the three seasons. The scatterplots for the three seasons show a similar pattern when $\tau_{0.55} < 0.6$, while for $\tau_{0.55} > 0.6$, the SWARF values from spring and winter seasons are higher than that of the summer season. The aerosol forcing efficiency, that is defined as the mean SWARF of the season divided by the mean $\tau_{0.55}$ of the season, are: −72, −73, and −70 W m^{-2} per $\tau_{0.55}$ for the winter, spring and summer seasons, respectively. Also shown in Figure 2 by the thick black line is a second-order polynomial fit for all three seasons where SWARF = $0.05 - 74.6\tau_{0.55} + 18.2\tau_{0.55}^2$ W m^{-2}. The slope of $\tau_{0.55}$ versus SWARF in this study is higher than previously reported in the work of *Christopher and Zhang*, [2002] where SWARF was studied

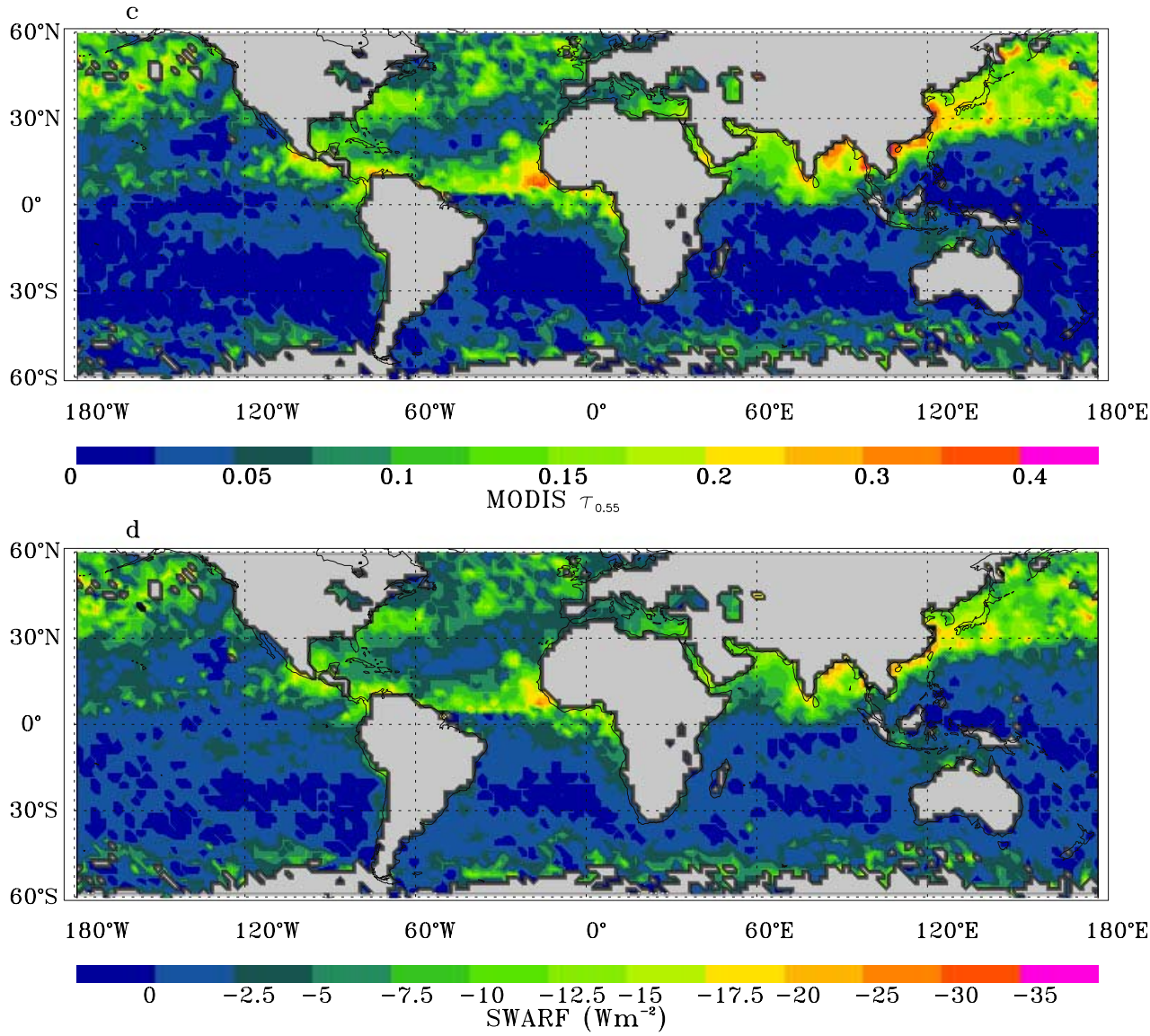

Figure 1. (continued)

over cloud-free global oceans using collocated MODIS and CERES data for only September 2000. The difference in slopes in the two studies is possibly due to the seasonal difference in aerosol distributions, ADMs, and cloud masking issues [*Zhang et al.*, 2005].

[13] There are, however, significant seasonal differences in the spatial distribution of $\tau_{0.55}$, and SWARF. For winter (Figures 1a and 1b), the dominant aerosol plumes are off the west coast of Africa, and Asia. Over the west coast of Africa, during this season, aerosols are from both wind-driven dust aerosols originating from desert areas [*Prospero et al.*, 2002], and smoke aerosols from biomass burning around 10° latitude [*Husar et al.*, 1997] while over India and China, pollutant aerosols dominate [*Ramanathan et al.*, 2001]. During spring (Figures 1c and 1d), the predominant aerosols are located in the Northern Hemisphere (NH) along the west coast of Africa, and India. The strong dust plumes originating from Asia are transported over the North Pacific Ocean and are observed at the west coast of North America (Figures 1c and 1d). During summer (Figures 1e and 1f), except for the persistent dust plumes over the west coast of north Africa, thick biomass burning plumes are observed over both east and west coast of South America when large fire episodes occur [*Swap et al.*, 2003].

[14] Since the aerosol forcing has a strong seasonal and regional dependence we identified ten selected regions to examine the instantaneous SWARF. The ten selected regions including north Africa (NA), southwest Africa (SWA), southeast Africa (SEA), Central America (CA), eastern United States (EUS), India, China, northwest Pacific (NWP), northeast Pacific (NEP), and Australia (AU) (Table 1) that are dominated by different types of aerosols. Over NA and SWA regions, the highest SWARF values of -9.7 and -9.3 W m^{-2} are found during summer corresponding to the highest MODIS $\tau_{0.55}$ value of 0.14 for both regions. For NA region, smaller SWARF values of -8.5 and -7.0 W m^{-2} are found during spring and winter. The dominant aerosol type over NA region is the trans-

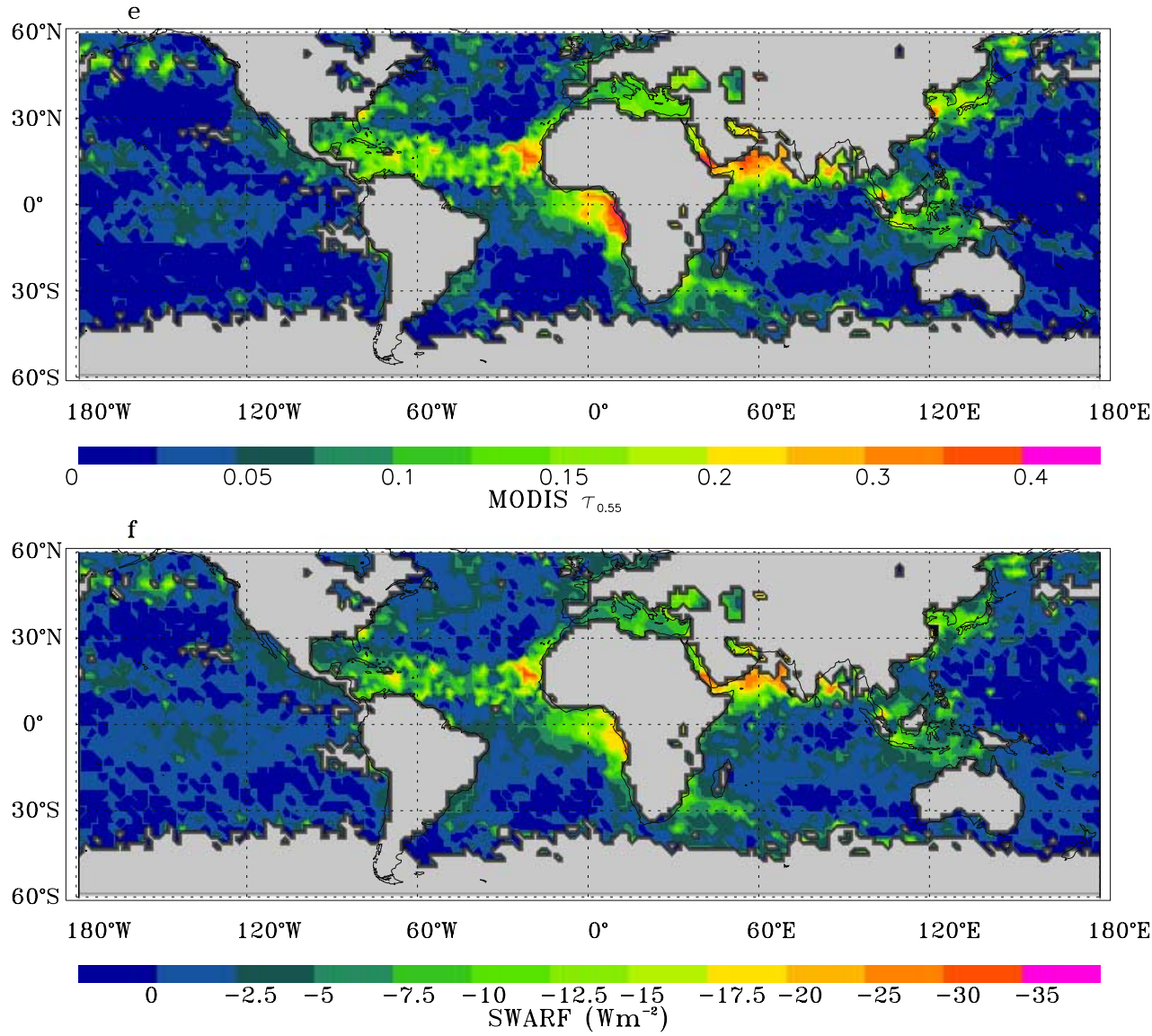

Figure 1. (continued)

ported dust aerosol originating from the Saharan deserts [e.g., *Prospero et al.*, 2002]. The high SWARF values over NA region for all three regions indicate the persistent dust SW cooling effect over that region. For SWA region, during spring, no significant aerosol plumes are apparent in Figure 1, and SWARF is as low as -5.5 W m^{-2}. During winter, due to the biomass burning activities in South Africa that typically starts around August and lasts until November [*Swap et al.*, 2003], the SWARF in SWA region increases to -8.2 W m^{-2}.

[15] Over India and China, the mean instantaneous SWARF reaches high values of -14.0 and -16.6 W m^{-2} during spring. High SWARF values are also found during summer and remain high through the winter for both of the regions. The fraction of fine mode to the total aerosol optical depth, as indicated by η is high for India where fine mode aerosol dominates the spring and winter seasons while coarse mode aerosols such as dust aerosols transported from NA region, dominate the summer season. Over China, the fine mode aerosols dominate at all seasons, although during spring the η value is the lowest. Similarly, the highest SWARF values of -14.9 and -10.9 W m^{-2} are also found over NWP and NEP regions for the same period. It is interesting to note that SWARF values are gradually reduced from source to NWP and NEP, which possibly indicates the direction of aerosol transport. In other two seasons, both NWP and NEP regions have low SWARF values. Also, during spring, both CA and EUS have high $\tau_{0.55}$ and SWARF values compared with other seasons. Over CA, the SWARF values are -7.0, -10.5 and -6.1 W m^{-2} for summer, spring and winter, respectively. The high SWARF and $\tau_{0.55}$ values during spring are associated with biomass burning events during that season over Central America [*Christopher et al.*, 2000].

[16] Figure 3 shows the zonal mean SWARF over cloud-free oceans calculated from the time of the satellite overpass. In the Southern Hemisphere (SH), the minimum SWARF values are found near $-20°$ to $-40°$ latitude with

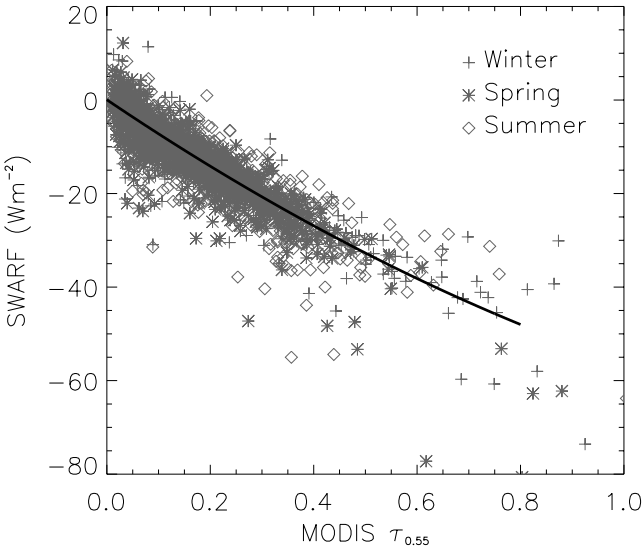

Figure 2. Scatterplot of MODIS $\tau_{0.55}$ versus CERES derived SWARF for the three seasons.

a SWARF peak of -7.5 W m^{-2} between $-40°$ and $-60°$N. These peak values are associated with the "roaring 40s" where strong winds injects large amount of sea salt aerosols into the air [*Fitzgerald*, 1991]. In the Northern Hemisphere (NH), two SWARF peaks are observed, one at 0°–20°N and another at 40°–50°N. The first is associated with the dust and biomass aerosols originating from north Africa that are transported around the equatorial region [*Prospero et al.*, 2002; *Swap et al.*, 2003]. The latter is associated with anthropogenic and dust aerosols originating from Asia that are transported across the Pacific Ocean [*Huebert et al.*, 2003]. The mean SWARF over SH is -5.3 W m^{-2}, and is lower than the averaged value of -7.9 W m^{-2} for the NH. *Chou et al.* [2002] also found a higher SWARF value over NH although the ratio of NH to SH SWARF values is smaller to those reported in the work of *Chou et al.* [2002] but similar to the values reported by *Loeb and Kato* [2002]. The mean $\tau_{0.55}$ for SH and NH over CERES cloud-free skies are 0.07 and 0.11, respectively. Although both $\tau_{0.55}$ and SWARF show a hemispheric difference, the instantaneous SW aerosol forcing efficiency (SWARF/$\tau_{0.55}$) is similar for both the NH and SH and is on the order of -70 W m^{-2} per $\tau_{0.55}$.

[17] In MODIS aerosol retrieval over oceans, the ratio (η) of fine mode to total $\tau_{0.55}$ is also derived and has been used for separating dust from other aerosols [*Kaufman et al.*, 2005; *Christopher and Zhang*, 2004]. Therefore we studied the effect of η to SWARF by dividing the data into two broad groups. The first group of data has $\eta > 0.8$ and mostly represents fine mode aerosols from pollution and biomass burning and the second group of data has $\eta < 0.6$ and represents aerosols largely from dust and sea salt aerosols [*Kaufman et al.*, 2005]. The seasonal mean MODIS $\tau_{0.55}$, SWARF, and SW forcing efficiency (defined as SWARF/$\tau_{0.55}$) for the three seasons for $\eta < 0.6$ and $\eta > 0.8$ are shown in Table 2. Both $\tau_{0.55}$ and SWARF show a larger variation for all three seasons when $\eta < 0.6$ compared to the cases when $\eta > 0.8$. For example, when $\eta < 0.6$, SWARF varies from -5.1 to -7.5 W m^{-2} for all three seasons while SWARF values have a smaller variation of -4.0 to -5.1 W m^{-2} for $\eta > 0.8$. Furthermore, in all three seasons, the aerosol forcing efficiency is smaller for $\eta > 0.8$ comparing with data for $\eta < 0.6$. Small η values relate to large particles such as sea salt and dust particles [*Tanré et al.*, 1997; *Kaufman et al.*, 2005] while larger η values relate to smaller particles like smoke and pollutant aerosols [*Tanré et al.*, 1997; *Kaufman et al.*, 2005]. Table 2 shows that smaller particles have a smaller aerosol forcing efficiency comparing with dust and sea salt particles and are consistent with the results of *Christopher and Zhang* [2002].

[18] Besides η, solar zenith angle (θ_o) is also another important factor that affects the derived SWARF. Figure 4 shows the variation in CERES SW flux as functions of $\tau_{0.55}$ and cosθ_0. A total of four cosθ_o ranges are studied: 0.9–1, 0.8–0.9, 0.7–0.8 and 0.6–0.7. The slope of $\tau_{0.55}$ versus SW flux increases as cos θ_o decreases. The highest slope of 79 W m^{-2} per $\tau_{0.55}$ is found for cos θ_o range of 0.6–0.7 and the lowest slope of 61 W m^{-2} per $\tau_{0.55}$ is found for cos θ_o ranges of 0.9–1.0. The difference in θ_o could induce a 10 W m^{-2} or higher difference in SWARF for $\tau_{0.55}$ value of 0.6 because as θ_o increases, the slant path also increases, and the incoming energy interacts with aerosols over a longer path. Assuming aerosol properties are independent of θ_o, a 10° change in θ_o could induce a 7–10% change in the SWARF over global oceans.

[19] The effect of solar zenith angle on SWARF is important because it is one of the factors that are needed to compare the SWARF derived from satellite to the numerical modeling studies. The numerical modeling results estimate the diurnally averaged SWARF while sat-

Table 1. Regional Averaged $\tau_{0.55}$ and Instantaneous SWARF for Three Seasons for Selected Regions

			NDJF		Spring		Summer	
	Latitude, °N	Longitude, °E	$\tau_{0.55}$	SWARF, W m^{-2}	$\tau_{0.55}$	SWARF, W m^{-2}	$\tau_{0.55}$	SWARF, W m^{-2}
NA	10–30	−60 to −10	0.10	−7.0	0.12	−8.5	0.14	−9.7
SWA	−20 to −5	−20–20	0.11	−8.2	0.08	−5.5	0.14	−9.3
SEA	−30 to −10	30–60	0.07	−5.0	0.05	−3.9	0.09	−6.9
CA	10–30	−120 to −80	0.08	−6.1	0.15	−10.5	0.11	−7.0
EUS	30–45	−80 to −50	0.07	−5.0	0.14	−10.1	0.09	−6.2
INDIA	0–30	60–100	0.15	−10.6	0.20	−14.0	0.16	−12.3
CHINA	20–40	110–150	0.16	−12.1	0.23	−16.6	0.12	−8.3
NWP	30–50	150–180	0.11	−7.5	0.20	−14.9	0.07	−4.9
NEP	30–50	−180 to −130	0.09	−5.8	0.15	−10.9	0.06	−4.8
AU	−20–0	100–150	0.08	−5.7	0.07	−5.0	0.10	−7.3

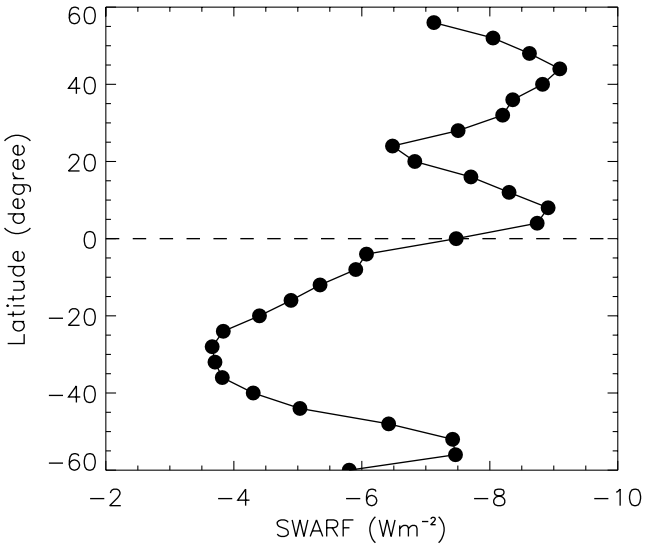

Figure 3. Ten-month zonal mean SWARF for Northern and Southern Hemispheres.

ellite studies provide SWARF at a given overpass time. The diurnally averaged SWARF is different from the instantaneous SWARF derived during satellite overpass time due to two main factors: the variations of θ_o and aerosol optical properties during a day. As suggested by *Kaufman et al.* [2000], Terra satellite measurements acquired during a specific overpass time could represent the daily averaged aerosol optical properties with a 2% error on the annual average. Therefore the major difference in satellite-derived SWARF and the diurnal averaged SWARF depends on the changes in θ_o during a day.

[20] We estimated the scaling factor between diurnal averaged SWARF and the SWARF obtained during the Terra overpass as follows. The mean θ_o values are first computed for every hour and every second month, for four latitude belts centered at 15°N, 15°S, 45°N, and 45°S. A four-stream radiative transfer model [*Fu and Liou*, 1993] was then used to compute the SWARF at different θ_o values. Since we do not have aerosol type information and the wavelength-dependent properties for each grid point, a total of 12 aerosol models are used in the calculations including maritime (MARI), continental (CONT), urban (URBA) [*D'Almeida et al.*, 1991], insoluble (INSO), water soluble (WASO), sea salt in accumulation mode (SSAM) and coarse mode (SSCM), mineral dust in nucleation (MINM), accumulation (MIAM), coarse (MICM), and transported (MITR) modes, and sulfate droplets (SUSO) [*Hess et al.*, 1998] and a $\tau_{0.55}$ value of 0.15 is assumed in the calculations with aerosol scale height of 4 km and a tropical atmospheric profile.

[21] To compute the scaling factor, the SWARF is first computed for each θ_o. The scaling factor is then calculated by dividing the 24-hour mean SWARF by the SWARF value that is computed at Terra overpass time (1030 LT). Table 3 lists the scaling factor for yearly mean for four latitude belts and for 12 different aerosols models. Also listed in Table 3 are the scaling factors averaged over all four latitude belts. As shown in Table 3, except for MICM that has very high absorption values in the shortwave, the scaling factors calculated from the other 11 aerosol models are clustered around 2 and have a mean of 2.0 and a standard deviation of 0.1. Therefore we assume a scaling factor of 2 to scale the instantaneous SWARF derived at the Terra over pass time to 24 hour averaged SWARF. Note that *Bellouin et al.* [2003] used theoretical radiative transfer calculations and estimated the scaling factors using integration on solar zenith angles, with a dependence on latitude and day of the year. However, in our study, the scaling factor that is also a strong function of aerosol models, is hard to estimate on a daily and regional basis. Therefore, in this study, only one scaling value is applied to the global oceans.

[22] Table 4 lists the seasonally averaged SWARF over global oceans (within ±60° latitude) estimated using ERBE, TRMM and Terra aerosol ADMs. Also listed in Table 4 are the mean SWARF values for the study period. Using Terra aerosol ADMs, the mean instantaneous SWARF over the oceans is -6.4 W m^{-2} and the corresponding values from the ERBE and TRMM ADMs s are -7.2 and -5.6 W m^{-2}, respectively. The SWARF value derived using Terra ADMs is within the SWARF values derived using ERBE and TRMM ADMs and is consistent with the results of *Zhang et al.* [2005] who indicated that the SWARF values derived from ERBE and TRMM ADMs serve as the upper and lower bound for the satellite-derived SWARF for uncertainties due to aerosol ADMs.

[23] The SWARF derived from this study, however, is biased toward CERES cloud-free skies. Because of the difference in the field of view, the averaged MODIS $\tau_{0.55}$ for CERES cloud-free ocean skies is 0.09 and the averaged MODIS $\tau_{0.55}$ is 0.15. Considering an aerosol forcing efficiency of 70 W m$^{-2}/\tau_{0.55}$, the SWARF corrected for this bias is -10.6 W m^{-2} [-70 W m$^{-2}/\tau_{0.55} \times (0.15-0.09)$ $-$ 6.4 W m^{-2}]. The mean aerosol forcing efficiency of 70 W m^{-2} per $\tau_{0.55}$ is obtained for $\tau_{0.55}$ between 0 to 0.4 and therefore, represents the global mean aerosol forcing efficiency at the range of $\tau_{0.55}$ from 0.09 to 0.15. The diurnally averaged SWARF, after accounting for the effect of solar zenith angle and clear-sky biases, is estimated to be -5.3 W m^{-2} over cloud-free oceans. Recall that to correct for the clear sky bias, the mean aerosol forcing efficiency of 70 W m^{-2} per $\tau_{0.55}$ is used. However, as shown in Table 2, the variations in η could introduce a 10% uncertainty in the mean aerosol forcing efficiency that will further introduce a 5% uncertainty in the diurnally averaged SWARF over cloud-free oceans.

[24] The 10-month averaged instantaneous and diurnally averaged SWARF over cloud-free oceans estimated from this study are -6.4 and -5.3 W m^{-2}, respectively. Notice that the first number is the instantaneous SWARF without

Table 2. MODIS and CERES Derived Aerosol and Flux Values As Function of Season

	$\eta > 0.8$			$\eta < 0.6$		
	$\tau_{0.55}$	SWARF, W m^{-2}	SWARF/$\tau_{0.55}$	$\tau_{0.55}$	SWARF, W m^{-2}	SWARF/$\tau_{0.55}$
Winter	0.060	−3.97	−66.2	0.091	−6.82	−75.0
Spring	0.066	−4.59	−69.6	0.100	−7.50	−75.0
Summer	0.075	−5.11	−68.1	0.073	−5.11	−70.0

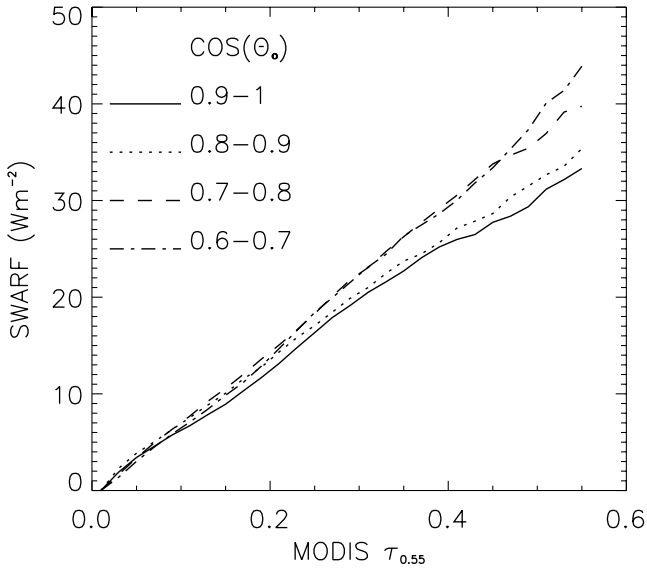

Figure 4. The averaged MODIS $\tau_{0.55}$ versus CERES as a function of cosine of solar zenith angle.

correcting for clear sky sample bias and the second number is the SWARF value after correcting for clear sky bias and accounting for the diurnal variation of solar zenith angle. The instantaneous SWARF derived over Terra over pass time is comparable to values reported by *Christopher and Zhang* [2002], where instantaneous SWARF of -6 W m^{-2} was obtained over cloud-free oceans for September 2000. The diurnally averaged SWARF of -5.3 W m^{-2} over global oceans derived in this study is comparable to, with a magnitude of less than 1 W m^{-2} differences to other studies using either a radiative transfer model, GCM, or satellite observations. For example, *Yu et al.* [2004] estimated the diurnal averaged SWARF of -4.6 W m^{-2} using MODIS aerosol retrieval and the Georgia Tech/Goddard Global Ozone Chemistry Aerosol Radiation Transport (GOCART) model. *Bellouin et al.* [2003] reported SWARF values of -5.2 W m^{-2} using the Polarization and Directionality of the Earth Reflectance (POLDER) observations and a radiative transfer model. Using the Sea-Viewing Wide Field-of-view Sensor (SeaWiFS) satellite retrievals, *Chou et al.* [2002] calculated a SWARF value of -5.4 W m^{-2} using a radiative transfer model. The diurnally averaged SWARF found in this study is similar to values reported (-4.6 W m^{-2}) by *Loeb and Kato* [2002] using 9 month averaged VIRS and CERES data over cloud-free tropical oceans. However, these values are lower than the -6.7 W m^{-2} values reported by *Haywood et al.* [1999], who compared annual mean cloud-free ERBE observations with GCM modeled results. In the work of *Haywood et al.* [1999], ERBE cloud-free data are used, and since possible cloud contamination of 0–5% exists in this data set [*Wielicki and Green*, 1989], this could be responsible for the high values of SWARF.

Table 3. Scaling Factors to Convert Instantaneous to Diurnally Averaged Values Estimated Using 12 Different Aerosol Models

	30–60°S	0–30°S	0–30°N	30–60°N	Global Mean
SUSO	2.22	1.85	2.00	2.18	2.06
MITR	2.10	1.67	1.83	2.06	1.92
MARI	2.17	1.78	1.94	2.14	2.01
INSO	1.97	1.36	1.58	1.93	1.71
WASO	2.30	1.96	2.10	2.27	2.16
SSAM	2.17	1.80	1.95	2.14	2.01
SSCM	2.11	1.71	1.87	2.08	1.94
MINM	2.26	1.92	2.06	2.23	2.12
MIAM	2.15	1.75	1.90	2.11	1.98
CONT	2.31	1.97	2.11	2.28	2.17
URBA	2.31	1.96	2.10	2.28	2.16
MICM	1.51	0.15	0.58	1.45	0.92

Table 4. Aerosol Direct Forcing Over CERES Cloud-Free Oceans Estimated Using Three Different ADMs

	NDJF, W m^{-2}	Spring, W m^{-2}	Summer, W m^{-2}	10 Months, W m^{-2}
ERBE ADMs	−7.1	−7.8	−6.7	−7.2
TRMM ADMs	−5.5	−6.1	−5.1	−5.6
Terra ADMs	−6.3	−6.9	−5.9	−6.4

4. Uncertainty Analysis

[25] The uncertainties in the SWARF value are primarily from four major sources including uncertainties in calibrated CERES radiances, uncertainties in converting filtered to unfiltered radiance, uncertainties in F_{clr} due to MODIS aerosol retrievals, and uncertainties in aerosol ADM methods. Although cloud contamination has been reported as a source of error from VIRS [*Loeb and Kato*, 2002] the stringent cloud-screening criteria and the use of high spatial and spectral resolution MODIS data used in this study eliminates most of the cloud contamination problems. Furthermore, in deriving SWARF since the difference in clear and observed fluxes is used, partial cancellation of cloud fraction exists and therefore the uncertainty in cloud contamination is assumed to be negligible.

[26] *Wielicki et al.* [1996] showed that the uncertainties in calibrated CERES SW radiance is on the order of 1%, corresponding to 0.8 W m^{-2} in the averaged SW flux over cloud-free oceans. *Loeb et al.* [2001] estimated the uncertainties in converting filtered to unfiltered radiance to be ~1%, or ~0.8 W m^{-2} over cloud-free oceans. The F_{clr} is derived using the regression relation between $\tau_{0.55}$ and SW flux for all CERES pixels that have $\tau_{0.55} < 0.2$ where the mean value of slope of the regression relation is 70 W m^{-2} per $\tau_{0.55}$. Therefore a 0.03 uncertainty in MODIS $\tau_{0.55}$ will induce a 2 W m^{-2} uncertainty in F_{clr}. The uncertainties in SWARF due to ADMs can be estimated from SWARF values that are derived using ERBE and TRMM ADMs. While SWARF derived from ERBE ADMs provides the lower bound, and the SWARF value derived from TRMM ADM provides the upper bound for the SWARF study using CERES observations. In this study, the mean SWARF is -7.2, -5.6 and -6.4 W m^{-2} using ERBE, TRMM and Terra aerosol ADMs. Therefore the uncertainties in SWARF due to ADMs is 0.8 W m^{-2}.

[27] Assuming the four main sources of uncertainties are not correlated, the total uncertainty in Terra ADMs can be estimated using equation (2) [*Penner et al.*, 1994]:

$$U_t = \exp\left[\sum (\log U_i)^2\right]^{1/2}, \quad (2)$$

where U_i is the uncertainty factor from each individual source of uncertainty and U_t is the total uncertainty factor. A 2% uncertainty is equivalent to an uncertainty factor value of 1.02. Combining all four sources of uncertainties, the averaged uncertainty in the instantaneous cloud-free sky CERES flux of 2.6 W m^{-2}. Two sources of uncertainties arise when converting the instantaneous SWARF to a diurnally averaged SWARF value including the uncertainty in the scaling factor (±0.1), and uncertainty in correcting the CERES clear sky bias for the global mean AOT (±0.03). We estimate the combined uncertainties from our analysis to be 1.7 W m^{-2}.

5. Conclusion

[28] Using 10 month of CERES SSF data, we have estimated the TOA SWARF over cloud-free oceans. The new Terra aerosol ADMs that are a significant improvement when compared to previous studies are used for inverting CERES SW radiances to fluxes that account for the variations in TOA SW radiance angular distribution patterns due to aerosols optical properties and near surface wind speed. The spatial and seasonal features of MODIS $\tau_{0.55}$ correspond well with the high SWARF values derived from CERES. The major results of this study are as follows:

[29] 1. Averaged over 10 months of data, the relationship between the instantaneous MODIS $\tau_{0.55}$ and SWARF estimated from two independent instruments can be represented by the following equation:

$$\mathrm{SWARF} = 0.05 - 74.6\tau_{0.55} + 18.2\tau_{0.55}^2 \mathrm{Wm}^{-2} (\tau_{0.55} < 0.8).$$

[30] 2. Averaged over global oceans, the instantaneous SWARF from Terra overpass is -6.4 ± 2.6 W m^{-2} and the diurnally averaged SWARF over cloud-free oceans is estimated to be -5.3 ± 1.7 W m^{-2}. The difference from -6.4 to -5.3 W m^{-2} is due to both the differences from instantaneous to diurnally averaged SWARF values and the correction for clear-sky bias. The instantaneous SWARF estimated from this study is similar to the estimations from one month of CERES and MODIS analysis [*Christopher and Zhang*, 2002]. The diurnally averaged SWARF is well within the range of values estimated by previous studies [*Loeb and Kato*, 2002; *Boucher and Tanré*, 2000; *Chou et al.*, 2002; *Yu et al.*, 2004].

[31] 3. This study does not use a radiative transfer model to calculate the SWARF from satellite-retrieved AOT. Rather it uses measured broadband radiances and an empirical ADM to retrieve fluxes at the TOA and is therefore an independent estimate of aerosol radiative forcing.

[32] 4. The aerosol forcing efficiency (SWARF/ $\tau_{0.55}$) is sensitive to the η factor, which is the ratio of small mode to coarse mode aerosol optical depth retrieved from MODIS. The aerosol forcing efficiency is higher when $\eta < 0.6$ compared to cases where $\eta > 0.8$ for all three seasons. The η factor has been used in separating dust from other aerosols [*Kaufman et al.*, 2005; *Christopher and Zhang*, 2004], and could be used in studying SWARF due to anthropogenic aerosols.

[33] **Acknowledgments.** This research was supported by NASA's Radiation Sciences, EOS Interdisciplinary Sciences, and ACMAP programs. Jianglong Zhang was supported by the NASA Earth System Science Fellowship and NASA AEROCENTER visiting scientist program. The CERES data were obtained from the NASA Langley Research Center Atmospheric Sciences Data Center, the MODIS data were obtained through the Goddard Space Flight Center Data Center, and the SSMI data were obtained from National Space and Science Technology Center (NSSTC), Huntsville, Alabama.

References

Ackerman, S. A., and H. Chung (1992), Radiative effects of airborne dust on regional energy budgets at the top of the atmosphere, *J. Appl. Meteorol.*, *31*, 223–233.

Bellouin, N., O. Boucher, D. Tanré, and O. Dubovik (2003), Aerosol absorption over the clear-sky oceans deduced from POLDER-1 and AERONET observations, *Geophys. Res. Lett.*, *30*(14), 1748, doi:10.1029/2003GL017121.

Boucher, O., and D. Tanré (2000), Estimation of the aerosol perturbation to the Earth's radiative budget over oceans using POLDER satellite aerosol retrievals, *Geophys. Res. Lett.*, *27*(8), 1103–1106.

Chou, M., P. Chan, and M. Wang (2002), Aerosol radiative forcing derived from sea WiFS-retrieved aerosol optical properties, *J. Atmos. Sci.*, *59*, 748–757.

Christopher, S. A., and J. Zhang (2002), Shortwave Aerosol Radiative Forcing from MODIS and CERES observations over the oceans, *Geophys. Res. Lett.*, *29*(18), 1859, doi:10.1029/2002GL014803.

Christopher, S. A., and J. Zhang (2004), Cloud-free shortwave aerosol radiative effect over oceans: Strategies for identifying anthropogenic forcing from Terra satellite measurements, *Geophys. Res. Lett.*, *31*, L18101, doi:10.1029/2004GL020510.

Christopher, S. A., J. Chou, J. Zhang, X. Li, and R. M. Welch (2000), Shortwave direct radiative forcing of biomass burning aerosols estimated from VIRS and CERES, *Geophys. Res. Lett.*, *27*, 2197–2200.

D'Almeida, G. A., P. Koepke, and E. P. Shettle (1991), *Atmospheric Aerosols—Global Climatology and Radiative Characteristics*, 561 pp., A. Deepak Publishing, Hampton, Va.

Fitzgerald, J. W. (1991), Marine aerosols: A review, *Atmos. Environ. Part A*, *25*, 533–545.

Fu, Q., and K. N. Liou (1993), Parameterization of the radiative properties of cirrus clouds, *J. Atmos. Sci.*, *50*, 2008–2025.

Hansen, J., M. Sato, A. Lacis, R. Ruedy, I. Tegen, and E. Matthews (1998), Climate forcings in the industrial era, *Proc. Natl. Acad. Sci.*, *95*, 12,753–12,758.

Haywood, J. M., V. Ramaswamy, and B. J. Soden (1999), Tropospheric aerosol climate forcing in clear-sky satellite observations over the oceans, *Science*, *283*, 1299–1303.

Hess, M., P. Koepke, and I. Schult (1998), Optical properties of aerosols and clouds: The software package OPAC, *Bull. Am. Meteorol. Soc.*, *79*, 831–844.

Huebert, B. J., T. Bates, P. B. Russell, G. Shi, Y. J. Kim, K. Kawamura, G. Carmichael, and T. Nakajima (2003), An overview of ACE-Asia: Strategies for quantifying the relationships between Asian aerosols and their climatic impacts, *J. Geophys. Res.*, *108*(D23), 8633, doi:10.1029/2003JD003550.

Husar, R. B., J. M. Prospero, and L. L. Stowe (1997), Characterization of tropospheric aerosols over the oceans with the NOAA advanced very high resolution radiometer optical thickens operational product, *J. Geophys. Res.*, *102*(D14), 16,889–16,909.

Intergovernmental Panel on Climate Change (IPCC) (2001), *Climate Change 2001: The Scientific Basis*, edited by J. T. Houghton et al., Cambridge Univ. Press, New York.

Kaufman, Y. J., B. N. Holben, D. Tanré, I. Slutzker, T. F. Eck, and A. Smirnov (2000), Will aerosol measurements from Terra and Aqua polar orbiting satellites represent the daily aerosol abundance and properties, *Geophys. Res. Lett.*, *23*, 3861–3864.

Kaufman, Y. J., I. Koren, L. Remer, D. Tanré, P. Ginoux, and S. Fan (2005), Dust transport and deposition observed from the Terra-MODIS spacecraft over the Atlantic Ocean, *Bull. Am. Meteorol. Soc*, in press.

King, M. D., Y. J. Kaufman, W. P. Menzel, and D. Tanre (1992), Remote Sensing of cloud, aerosol, and water vapor properties from the Moderate Resolution Imaging Spectrometer (MODIS), *IEEE Trans. Geosci. Remote Sens.*, *30*, 2–27.

Loeb, N. G., and S. Kato (2002), Top-of-atmosphere direct radiative effect of aerosols from the Clouds and the Earth's Radiant Energy System Satellite instrument (CERES), *J. Clim.*, *15*, 1474–1484.

Loeb, N. G., et al. (2001), Determination of unfiltered radiances from the Clouds and the Earth's Radiant Energy System (CERES) instrument, *J. Appl. Meteorol.*, *40*, 822–835.

Loeb, N. G., et al. (2003), Angular distribution models for Top-of-Atmosphere radiative flux estimation from the Clouds and the Earth's Radiant Energy System instrument on the Tropical Rainfall Measur-

ing Mission satellite. Part I: Methodology, *J. Appl. Meteorol.*, *42*, 240–265.

Penner, J. E., R. J. Charlson, S. E. Schwartz, J. M. Hales, N. S. Laulainen, L. Travis, R. Leifer, T. Novakov, J. Ogren, and L. F. Radke (1994), Quantifying and minimizing uncertainty of climate forcing by anthropogenic aerosols, *Bull. Am. Meteorol. Soc.*, *75*, 375–400.

Prospero, J. M., P. Ginoux, O. Torres, S. E. Nicholson, and T. E. Gill (2002), Environmental characterization of global sources of atmospheric soil dust identified with the NIMBUS 7 Total Ozone Mapping Spectrometer (TOMS) absorbing aerosol product, *Rev. Geophys.*, *40*(1), 1002, doi:10.1029/2000RG000095.

Ramanathan, V., et al. (2001), The Indian Ocean Experiment: An Integrated assessment of the climate forcing and effects of the Great Indo-Asian Haze, *J. Geophys. Res.*, *106*(D22), 28,371–28,399.

Remer, L. A., et al. (2002), Validation of MODIS aerosol retrieval over ocean, *Geophys. Res. Lett.*, *29*(12), 8008, doi:10.1029/2001GL013204.

Swap, R. J., H. J. Annegarn, J. T. Suttles, M. D. King, S. Platnick, J. L. Privette, and R. J. Scholes (2003), Africa burning: A thematic analysis of the Southern African Regional Science Initiative (SAFARI 2000), *J. Geophys. Res.*, *108*(D13), 8465, doi:10.1029/2003JD003747.

Tanré, D., Y. J. Kaufman, M. Herman, and S. Matto (1997), Remote sensing of aerosol properties over oceans using the MODIS/EOS spectral radiance, *J. Geophys. Res.*, *102*, 16,971–16,988.

Wielicki, B. A., and R. N. Green (1989), Cloud identification for ERBE radiative flux retrieval, *J. Appl. Meteorol.*, *28*, 1133–1146.

Wielicki, B. A., B. R. Barkstrom, E. F. Harrison, R. B. Lee III, G. L. Smith, and J. E. Cooper (1996), Clouds and the Earth's Radiant Energy System (CERES): An Earth Observing System Experiment, *Bull. Am. Meteorol. Soc.*, *77*, 853–868.

Yu, H., et al. (2004), Direct radiative effect of aerosols as determined from a combination of MODIS retrievals and GOCART simulations, *J. Geophys. Res.*, *109*, D03206, doi:10.1029/2003JD003914.

Zhang, J., S. A. Christopher, L. A. Remer, and Y. J. Kaufman (2005), Shortwave aerosol radiative forcing over cloud-free oceans from Terra: 1. Angular models for aerosols, *J. Geophys. Res.*, D10S23, doi:10.1029/2004JD005008.

S. A. Christopher, Department of Atmospheric Sciences, University of Alabama, 320 Sparkman Drive, Huntsville, AL 35805-1912, USA.

Y. J. Kaufman and L. A. Remer, Code 913, NASA Goddard Space Flight Center Data Center, Greenbelt, MD 20771, USA.

J. Zhang, Naval Research Laboratory, 7 Grace Hopper Ave., Stop 2, Monterey, CA 93943-5502, USA. (zhang@nrlmry.navy.mil)